A New Variational Method for Bias Correction and its Applications to Rodent Brain Extraction

Huibin Chang, Weimin Huang, Chunlin Wu, Su Huang, Cuntai Guan, Sakthivel Sekar, Kishore Kumar Bhakoo and Yuping Duan*

***Abstract*—Brain extraction is an important preprocessing step for further analysis of brain MR images. Significant intensity inhomogeneity can be observed in rodent brain images due to the high-field MRI technique. Unlike most existing brain extraction methods that require bias corrected MRI, we present a high-order and L_0 regularized variational model for bias correction and brain extraction. The model is composed of a data fitting term, a piecewise constant regularization and a smooth regularization, which is constructed on a 3-D formulation for medical images with anisotropic voxel sizes. We propose an efficient multi-resolution algorithm for fast computation. At each resolution layer, we solve an alternating direction scheme, all subproblems of which have the closed-form solutions. The method is tested on three T2 weighted acquisition configurations comprising a total of 50 rodent brain volumes, which are with the acquisition field strengths of 4.7 Tesla, 9.4 Tesla and 17.6 Tesla, respectively. On one hand, we compare the results of bias correction with N3 and N4 in terms of the coefficient of variations on 20 different tissues of rodent brain. On the other hand, the results of brain extraction are compared against manually segmented gold standards, BET, BSE and 3-D PCNN based on a number of metrics. With the high accuracy and efficiency, our proposed method can facilitate automatic processing of large-scale brain studies.**

***Index Terms*—Intensity inhomogeneity, brain extraction, high-field MRI, rodent brain, human brain, segmentation, multi-resolution**

I. Introduction

RODENT brains have been used as preclinical models to investigate brain development, disease progression and new drug discovery [1], [2], [3]. A common processing step of rodent MR images is to segment the brain tissue from non brain tissues such as cranium, eyes, muscles and skin *etc.*, which is usually called brain extraction/cropping or skull stripping.

Manuscript received October 13, 2016; revised November 30, 2016. *Asterisk indicates corresponding author.*

*Y. Duan is with Center for Applied Mathematics, Tianjin University, Tianjin, China 300072. E-mail: yuping.duan@tju.edu.cn.

H. Chang is with Department of Mathematical Sciences, Tianjin Normal University, Tianjin, China 300387.

W. Huang and S. Huang are with the Neural & Biomedical Technology Department, Institute for Infocomm Research, A*Star, Singapore 138632.

C. Guan is with Nanyang Technological University, 50 Nanyang Ave, Singapore 639798.

C. Wu is with School of Mathematical Sciences, Nankai University, Tianjin, China 300071.

S. Sekar and K. Bhakoo are with Singapore Bioimaging Consortium, Agency for Science, Technology and Research

Automated brain extraction methods are widely used for human brain extraction, such as region growing method[4], edge-based method [5], hybrid method [6] and expectation-maximization based method [7] *etc.*. However, the human brain extraction methods often perform poorly on rodent brains due to the diversities in shapes and the differences in image contrasts between human and rodent brains. In the last two decades, several methods have been proposed for rodent brain extraction either by modifying human brain methods or developing new approaches. The atlas-based expectation maximization techniques were studied and applied for murine full brain segmentation in [8], [9]. Uberti *et al.* [10] presented a semi-automatic method, called Contrast Level Set (CLS), which used a level set algorithm to evolve a user-defined initial surface toward to brain boundary. Murugavel and Sullivan [11] proposed a neural network based method, called Pulse-Coupled Neural Network (PCNN) to automatically crop rodent brain tissue. The PCNN algorithm was further extended in the 3-D formulation in [12] to overcome the limitation of 2-D PCNN in segmenting the anterior and posterior region of rodent volumes. Li *et al.* [13] proposed an automatic rat brain extraction method based on the deformable surface model used in Brain Extraction Tool (BET) [4]. Recently, Oguz *et al.* [14] introduced a rodent brain cropping method based on grayscale mathematical morphology and LOGISMOS-based graph segmentation.

High-field MRI is a popular technique for the study of rodent brains, in which obvious intensity inhomogeneity (bias) widely exists [15] and usually is a smooth intensity variation across the image. It arises from the imperfections of the image acquisition process and is induced by the choice of the radio-frequency coil, the acquisition pulse sequence and by the nature and geometry of the sample itself. Amongst the various bias correction methods, the most popular one is the nonparametric nonuniform normalization (N3) approach [16], which has established itself as a standard in the field. A modified method, N4, was proposed to improve the original N3 algorithm [17]. A good review of methods for correction of intensity inhomogeneity in MRI can be found in [18].

The intensity inhomogeneity is usually modeled as a smooth multiplicative field arising from variations in the sensitivity of the reception coil and to a lesser extent with the non-uniformity due to induced currents and nonuniform excitation [19]. Therefore, an observed image v can be modeled as

$$v(x) = \big(1 + n(x)\big) \times u(x) \times f(x), \tag{1}$$

where u is the uncorrupted image, f is the bias field and n is

the measurement error. Based on the logarithmic transformation, the image model (1) becomes

$$\hat{v}(x) = \hat{u}(x) + \hat{f}(x) + \hat{n}(x), \tag{2}$$

where $\hat{v} = \log v$, $\hat{u} = \log u$, $\hat{f} = \log f$ and $\hat{n} = \log\big(1+n(x)\big)$. Here, we make the following assumptions with respect to $\hat{u}$ and $\hat{f}$, respectively

(A1) The true image $\hat{u}$ characterizes a physical property of the tissues being imaged, which ideally has the same value for the voxels on the same type of tissue.

(A2) The bias field $\hat{f}$ is a spatially smooth function and usually follows certain paths, which can be modeled by a piecewise linear approximation.

A. Variational Methods for Bias Correction

The Mumford-Shah model is a well-known variational segmentation model by pursuing a piecewise smooth approximation of the given image and the boundaries are referred as the transition between adjacent pathes of the approximation [20]. One of the most successful relaxation models of the Mumford-Shah model was proposed by Chan and Vese [21], which seeks for an approximation of a given image with a binary piecewise constant representation trough a level set formulation. Many models and algorithms have been proposed for segmentation of images with intensity inhomogeneity based on the Mumford-Shah model and the Chan-Vese model. For example, Li *et al.* [22] defined the local binary fitting (LBF) model by introducing a kernel function into the data term of the Chan-Vese model to cope with intensity inhomogeneity. Li *et al.* [23] proposed a weighted k-means clustering with the cluster centers to estimate the bias function within the neighborhood. Later in [24], a local intensity clustering (LIC) property of the image intensities was derived and used for the segmentation of MR images in the presence of intensity inhomogeneity. Li *et al.* [25] developed a variational fuzzy Mumford-Shah model for image segmentation with the application to images with intensity inhomogeneity.

Another kind of variational models to correct intensity inhomogeneity are Retinex [26], which deals with inhomogeneity caused by different illumination conditions. Retinex theory and intensity inhomogeneity originate from the same assumptions based on the image decomposition model (1). Based on the well-known Total Variation (TV) [27], different TV models have been proposed for Retinex. Kimmel *et al.* [28] proposed a variational framework for Retinex based on the TV and H^1 regularization. Later, a variant of this model was proposed by Ng and Wang [29]. Ma *et al.* proposed a variational model to recover the piecewise constant function u with a data term in gradient field [30], [31]. Zosso *et al.* extended the TV models to a unified non-local formulation [32].

Although TV based models have been studied intensively, this kind of approaches suffers the so-called staircase effect. In order to suppress such effect, a number of high-order models have been established. Chambolle and Lions [33] proposed the infimal convolution by combining the first-order total variation and second-total variation, which was further studied in [34], [35]. The total generalized variation (TGV) was proposed and studied in [36], which also involved higher order derivatives. Recently, Liang and Zhang [37] used the high-order total variation L_1 decomposition to solve the Retinex problems, which decomposed the gradient field of images into salient edges and relatively smoother illumination field.

B. Our Contributions

In our previous work [38], we proposed a novel variational model for simultaneously bias correction and segmentation, called the L_0 regularized Mumford-Shah model (L0MS), which is closely related to the Mumford-Shah model as well. Let Ω be an index set, the L0MS model is defined based on the additive image model (2) as follows

$$\min_{\hat{u},\hat{f}} \sum_{\omega\in\Omega}\sum_{\varpi\in\mathcal{N}_\omega} \frac{1}{2}K\big(x(\omega)-x(\varpi)\big)\big(\hat{v}(\varpi)-\hat{u}(\varpi)-\hat{f}(\omega)\big)^2 + \frac{\mu}{2}\|\nabla\hat{f}\|^2 + \alpha\|\nabla\hat{u}\|_0, \tag{3}$$

where μ, α are positive parameters, K is a nonnegative weighting function, $\mathcal{N}_\omega$ is a neighborhood of the index ω, $\|\cdot\|$ denotes the L_2 norm and $\|\cdot\|_0$ denotes the L_0 norm.

In the functional (3), the first term measures the fidelity to the observed data. Unlike the Mumford-Shah model, we defined the data fidelity using the local intensity properties to allow the bias field to be influenced by its neighborhood. If we pursue the Euler-Lagrange equation of this term with respect to $\hat{f}$, we come up with $\hat{f} = K * (\hat{v} - \hat{u})$, where "*" denotes the convolution operation. The difference between $\hat{v}$ and $\hat{u}$ is exactly $\hat{f}$, which means we used a window function K to smooth the solution of $\hat{f}$. The second term imposes spatial smoothness on the bias field, which was derived from the Mumford-Shah model. Actually, minimizing $\|\nabla\hat{f}\|^2$ translates into the Euler-Lagrange equation $\Delta\hat{f} = 0$, the steepest decent solution of which is a Gaussian smoothing operation. It is obviously that these two terms share the same functions for the bias field $\hat{f}$. Moreover, when we consider 3-D problems such as rodent MRI segmentation, the computational costs of the convolution increase evidently due to the 3-D window function involved in the computation.

In this paper, we plan to improve our previous model (3) by modeling the bias field $\hat{f}$ based on a high-order regularization and design a new variational model for bias correction of MR images with significant intensity inhomogeneity. We call it as high-order and L_0 regularized Mumford-Shah model (HoL0MS), which is given as follows

$$\min_{\hat{u},\hat{f}} \quad \frac{1}{2}\|\hat{v}-\hat{u}-\hat{f}\|^2 + \frac{\mu}{2}\|H\hat{f}\|^2 + \alpha\|\nabla\hat{u}\|_0, \tag{4}$$

where H denotes the Hessian operator, a square matrix of second-order partial derivatives of $\hat{f}$, to be defined in Section II. Closely connected to our previous work, we use an L_0 gradient minimization to establish the discontinuity set with the minimal length and introduce a smooth regularizer by extracting high order singularities as the bias field. In the meantime, the data fitting term is simplified by removing the local kernel function. Both true intensity and bias field are estimated based on the HoL0MS model (4). Targeted for the applications in brain extraction, we model the true intensity

as a piecewise constant function, where a simple thresholding can isolate the brain region from non-brain regions. Certain morphological operations are required to accurately estimate the boundaries of the brain mask. Since the voxel size may not be isotropic in medical data sets, it is important to allow for non-uniform grid sizes. We construct the minimization problem in a fully 3-D formulation to be with global perspective. For fast computation, we design a multi-resolution algorithm with few relaxation iterations on each resolution layer. The processing flow is outlined in Fig. 1, while the high-order and L_0 regularized Mumford-Shah model is described in the following sections.

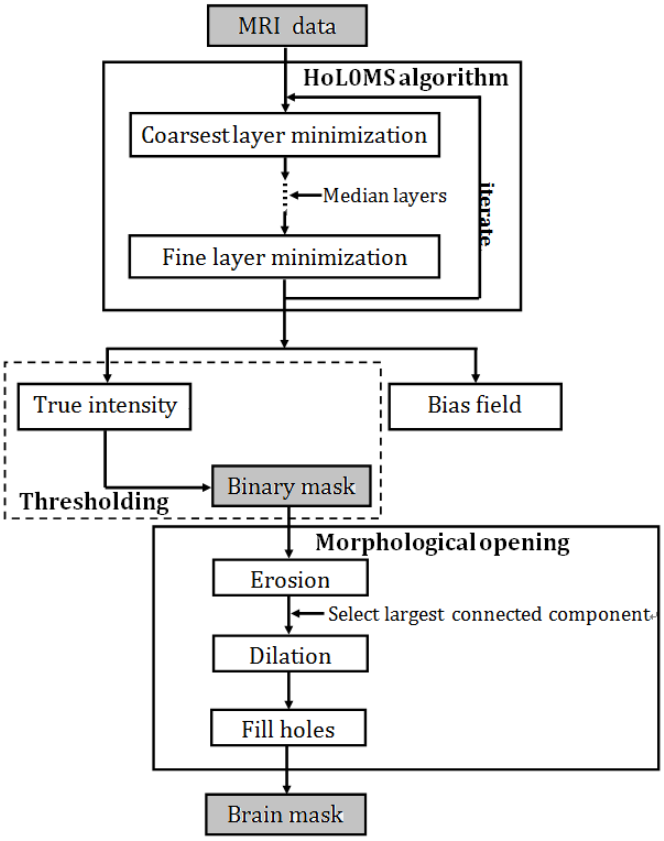

Fig. 1. Processing flow of the HoL0MS model for rodent brain extraction.

II. Notations

Without loss of generality, we represent a grayscale 3-D image as an $M \times N \times L$ tensor, that is $\Omega = \{1, 2, \cdots, M\} \times \{1, 2, ..., N\} \times \{1, 2, ..., L\}$. The Euclidean space $\mathbb{R}^{M\times N\times L}$ is denoted as V. The discrete grid points are given by $(x_i, y_j, z_k) = (i\Delta x, j\Delta y, k\Delta z)$, where Δx, Δy, Δz denote the spatial discretization steps. Here, Δx, Δy, Δz can be distinct with each other for anisotropic voxel sizes of the rodent MR images.

We will use the discrete backward and forward difference operators for $u \in V$ as follows

$$D_x^- u(i,j,k) = \begin{cases} \frac{u(i,j,k)-u(i-1,j,k)}{\Delta x} & 1 < i \le M, \\ \frac{u(1,j,k)-u(M,j,k)}{\Delta x} & i = 1. \end{cases}$$

$$D_y^- u(i,j,k) = \begin{cases} \frac{u(i,j,k)-u(i,j-1,k)}{\Delta y} & 1 < j \le N, \\ \frac{u(i,1,k)-u(i,N,k)}{\Delta y} & j = 1. \end{cases}$$

$$D_z^- u(i,j,k) = \begin{cases} \frac{u(i,j,k)-u(i,j,k-1)}{\Delta z} & 1 < k \le L, \\ \frac{u(i,j,1)-u(i,j,L)}{\Delta z} & k = 1. \end{cases}$$

$$D_x^+ u(i,j,k) = \begin{cases} \frac{u(i+1,j,k)-u(i,j,k)}{\Delta x} & 1 \le i < M, \\ \frac{u(1,j,k)-u(M,j,k)}{\Delta x} & i = M. \end{cases}$$

$$D_y^+ u(i,j,k) = \begin{cases} \frac{u(i,j+1,k)-u(i,j,k)}{\Delta y} & 1 \le j < N, \\ \frac{u(i,1,k)-u(i,N,k)}{\Delta y} & j = N. \end{cases}$$

$$D_z^+ u(i,j,k) = \begin{cases} \frac{u(i,j,k+1)-u(i,j,k)}{\Delta z} & 1 \le k < L, \\ \frac{u(i,j,1)-u(i,j,L)}{\Delta z} & k = L. \end{cases}$$

Here, we use the periodic boundary condition to define the difference operators, where u is periodically extended. Accordingly, the Fast Fourier Transform can be used in the algorithm. Indeed, other boundary conditions can be used as well, which haven been discussed in [39].

We define the gradient operator $\nabla : V \to P$, where $P = V \times V \times V$ in the discrete context

$$\nabla u(i,j,k) = \Big(D_x^+ u(i,j,k), D_y^+ u(i,j,k), D_z^+ u(i,j,k)\Big).$$

We define the discrete divergence operator $\mathrm{div} : P \to V$ for $\boldsymbol{p} = (p_1, p_2, p_3) \in P$ as

$$\mathrm{div}\boldsymbol{p}(i,j,k) = D_x^- p_1(i,j,k) + D_y^- p_2(i,j,k) + D_z^- p_3(i,j,k).$$

Next, we explicitly give the definition of H for $u \in V$ based on the second order difference operators as

$$Hu(i,j,k) = \begin{pmatrix} D_{xx}^{-+}u(i,j,k), & D_{xy}^{-+}u(i,j,k), & D_{xz}^{-+}u(i,j,k) \\ D_{yx}^{-+}u(i,j,k), & D_{yy}^{-+}u(i,j,k), & D_{yz}^{-+}u(i,j,k) \\ D_{zx}^{-+}u(i,j,k), & D_{zy}^{-+}u(i,j,k), & D_{zz}^{-+}u(i,j,k) \end{pmatrix}.$$

We also define the adjoint operator H^T for the above Hessian as

$$\begin{aligned} H^T\boldsymbol{q} = {} & D_{xx}^{+-}q_{11} + D_{yx}^{-+}q_{12} + D_{zx}^{-+}q_{13} + D_{xy}^{+-}q_{21} + D_{yy}^{-+}q_{22} \\ & + D_{zy}^{-+}q_{23} + D_{xz}^{+-}q_{31} + D_{yz}^{-+}q_{32} + D_{zz}^{-+}q_{33}, \end{aligned}$$

where

$$\boldsymbol{q} = \begin{pmatrix} q_{11} & q_{12} & q_{13} \\ q_{21} & q_{22} & q_{23} \\ q_{31} & q_{32} & q_{33} \end{pmatrix},$$

with $q_{i,j} \in V$, $i, j = 1, 2, 3$.

When discussing discretized problems, we shall frequently use vector norms to avoid cumbersome summation. Thus, $\forall \mathcal{S} \subseteq \Omega$, we define the following norm

$$\|u\|_{\mathcal{S}} = \Big(\sum_{\omega\in\mathcal{S}} |u(\omega)|^2\Big)^{\frac{1}{2}}.$$

If $\mathcal{S} = \Omega$, we simply denote the norm as $\|u\|$.

III. High order and L_0 regularized Mumford-Shah Model (HoL0MS)

We propose a novel variational model for bias correction and brain extraction as follows

$$\min_{\hat{u},\hat{f}} \Big\{\mathcal{E}(\hat{u},\hat{f}) := \frac{1}{2}\|\hat{v}-\hat{u}-\hat{f}\|^2 + \frac{\mu}{2}\|H\hat{f}\|^2 + \frac{\tau}{2}\|\hat{f}\|^2 + \alpha\|\nabla\hat{u}\|_0\Big\}, \tag{5}$$

where τ is a positive parameter. We explicitly define the L_0 measure of gradient as follows

$$\|\nabla\hat{u}\|_0 = \#\{\omega\in\Omega \;\big|\; |\partial_x\hat{u}(\omega)| + |\partial_y\hat{u}(\omega)| + |\partial_z\hat{u}(\omega)| \neq 0\}, \tag{6}$$

with $\#\{\cdot\}$ being the counting operator, which outputs the number of ω that satisfies $|\partial_x\hat{u}(\omega)|+|\partial_y\hat{u}(\omega)|+|\partial_z\hat{u}(\omega)| \neq 0$. It means the L_0 regularization on $\nabla\hat{u}$ counts the number of jumps of $\hat{u}$, which is able to promote a jump-sparse solution of $\hat{u}$. This property agrees with our assumption on $\hat{u}$ as a piecewise constant function.

The existence of the minimizer for (5) is given as follows.

Theorem 3.1. *There exist a pair* $(\hat{u}^*,\hat{f}^*)$*, which minimizes the proposed model* (5)*, i.e.*

$$(\hat{u}^*,\hat{f}^*) = \arg\min_{\hat{u},\hat{f}} \mathcal{E}(\hat{u},\hat{f})$$

Proof: Due to the lower semi-continuous property of term $\|\nabla(\cdot)\|_0$, one can readily prove this theorem. ∎

IV. Energy Minimization and Algorithm

In this section, we present the algorithm for solving the minimization problem (5). We first rewrite the minimization problem into the following constrained problem

$$\begin{aligned}\min_{\hat{u},\hat{f},\boldsymbol{p}} \;& \frac{1}{2}\|\hat{v}-\hat{u}-\hat{f}\|^2 + \frac{\mu}{2}\|H\hat{f}\|^2 + \frac{\tau}{2}\|\hat{f}\|^2 + \alpha\|\boldsymbol{p}\|_0 \\ \text{s.t.},\;& \boldsymbol{p} = \nabla\hat{u},\end{aligned} \tag{7}$$

where $\boldsymbol{p} = (p_1,p_2,p_3) \in P$.

To solve the constrained optimization problem (7), we rewrite it into the unconstrained minimization problem using the penalty method as follows

$$\min_{\hat{u},\hat{f},\boldsymbol{p}} \Big\{\mathcal{L}_\beta(\hat{u},\hat{f},\boldsymbol{p}) := \frac{1}{2}\|\hat{v}-\hat{u}-\hat{f}\|^2 + \alpha\|\boldsymbol{p}\|_0 + \frac{\mu}{2}\|H\hat{f}\|^2 + \frac{\tau}{2}\|\hat{f}\|^2 + \frac{\beta}{2}\|\boldsymbol{p}-\nabla\hat{u}\|^2\Big\}, \tag{8}$$

with a sufficiently large penalty parameter β. Since the three unknowns are coupled together in (8), an inner alternating scheme is used with respect to $\hat{u}$, $\hat{f}$ and $\boldsymbol{p}$, respectively. It seems one can prove the convergence in the sense that the limit of the subsequences of the iterative solutions is only the local minimizer to (5) following [40], [41]. More future work will be done to study how to describe the convergence behavior with respect to the global property [42].

A. Sub-Minimization with respect to $\hat{u}$

We obtain the sub-minimization problem w.r.t. the variable $\hat{u}$ as follows

$$\min_{\hat{u}} \; \frac{1}{2}\|\hat{v}-\hat{u}-\hat{f}\|^2 + \frac{\beta}{2}\|\boldsymbol{p}-\nabla\hat{u}\|^2. \tag{9}$$

The Euler-Lagrange equation of the $\hat{u}$-sub minimization problem (9) is given as

$$(\mathcal{I}-\beta\mathrm{div}\nabla)\hat{u} = \hat{v}-\hat{f}-\beta\mathrm{div}\boldsymbol{p}. \tag{10}$$

Using the discrete difference operators, we can rewrite the above equation as follows

$$\Big(\mathcal{I}-\beta(D_x^-D_x^+ + D_y^-D_y^+ + D_z^-D_z^+)\Big)\hat{u} = g,$$

where $g = \hat{v}-\hat{f}-\beta(D_x^-p_1 + D_y^-p_2 + D_z^-p_3)$. Since periodic boundary condition is imposed on $\hat{u}$, $D_x^-D_x^+$, $D_y^-D_y^+$ and $D_z^-D_z^+$ are block circulant and can be diagonalized by discrete Fourier transform [39]. Denoting $\mathcal{F}(\hat{u})$ as the Fourier transform of $\hat{u}$, we have

$$\Big(\mathcal{I}-\beta\big(\mathcal{F}(D_x^-)\mathcal{F}(D_x^+)+\mathcal{F}(D_y^-)\mathcal{F}(D_y^+)\big)\Big)\mathcal{F}(\hat{u}) = \mathcal{F}(g). \tag{11}$$

Here, the multiplication between the difference operators is componentwise according to the convolution theorem [43]. Let $\mathcal{G} = \mathcal{I}-\beta\big(\mathcal{F}(D_x^-)\mathcal{F}(D_x^+)+\mathcal{F}(D_y^-)\mathcal{F}(D_y^+)\big)$. By applying the discrete inverse Fourier transform $\mathcal{F}^{-1}$, we have the following closed-form solution to $\hat{u}$

$$\hat{u}^* = \mathcal{F}^{-1}\big(\mathcal{F}(g)/\mathcal{G}\big), \tag{12}$$

where $\cdot/\cdot$ denotes the componentwise division. The quantities including $\mathcal{G}$ and $\mathcal{F}(\hat{v})$ in (11) are constant and can be pre-computed. The main computational cost of $\hat{u}^*$ is one Fourier transform and one inverse Fourier transform in one iteration.

B. Sub-Minimization with respect to $\hat{f}$

We obtain the sub-minimization problem w.r.t. the variable $\hat{f}$ as follows

$$\min_{\hat{f}} \; \frac{1}{2}\|\hat{v}-\hat{u}-\hat{f}\|^2 + \frac{\mu}{2}\|H\hat{f}\|^2 + \frac{\tau}{2}\|\hat{f}\|^2. \tag{13}$$

By pursuing the Euler-Lagrange equation of $\hat{f}$-sub minimization problem (13), we have the following linear equation

$$\big((1+\tau)\mathcal{I}+\mu H^TH\big)\hat{f} = \hat{v}-\hat{u}, \tag{14}$$

with the periodic boundary condition. Since H^T and H are block circulant, we can solve (14) based on the FFT as well, which gives

$$\Big((1+\tau)\mathcal{I}+\mu\mathcal{F}(H^T)\mathcal{F}(H)\Big)\mathcal{F}(\hat{f}) = \mathcal{F}(\hat{v}-\hat{u}). \tag{15}$$

Let $\mathcal{J} = \big((1+\tau)\mathcal{I}+\mu\mathcal{F}(H^T)\mathcal{F}(H)\big)$. We have the following closed-form solution to $\hat{f}$

$$\hat{f}^* = \mathcal{F}^{-1}\Big(\mathcal{F}(\hat{v}-\hat{u})/\mathcal{J}\Big). \tag{16}$$

Similarly, since $\mathcal{J}$ and $\mathcal{F}(\hat{v})$ can be pre-computed, the main computational cost of $\hat{f}$ in (16) involves one Fourier transform and one inverse Fourier transform in one iteration.

C. Sub-Minimization with respect to $\boldsymbol{p}$

We obtain the sub-minimization problem w.r.t. the variable $\boldsymbol{p}$ as follows

$$\min_{\boldsymbol{p}} \quad \alpha\|\boldsymbol{p}\|_0 + \frac{\beta}{2}\|\boldsymbol{p} - \nabla\hat{u}\|^2. \tag{17}$$

According to the definition of L_0 norm (6), the minimization problem (17) can be spatially decomposed. For ease of illustration, we define the following binary function for $\boldsymbol{p}(\omega) = (p_1(\omega), p_2(\omega), p_3(\omega)), \forall\omega \in \Omega$

$$\mathcal{C}(\boldsymbol{p}(\omega)) = \begin{cases} 1, & |p_1(\omega)| + |p_2(\omega)| + |p_3(\omega)| \neq 0; \\ 0, & \text{otherwise.} \end{cases}$$

Relying on the above binary function, we are able to rewrite (17) as the following summation

$$\sum_{\omega} \min_{\boldsymbol{p}(\omega)} \Big\{\alpha\mathcal{C}(\boldsymbol{p}(\omega)) + \frac{\beta}{2}\big(\boldsymbol{p}(\omega) - \nabla\hat{u}(\omega)\big)^2\Big\}.$$

Thus, the optimal $\boldsymbol{p}^*$ can be solved individually by

$$\boldsymbol{p}^*(\omega) = \arg\min_{p(\omega)} \Big\{\alpha\mathcal{C}(\boldsymbol{p}(\omega)) + \frac{\beta}{2}\big(\boldsymbol{p}(\omega) - \nabla\hat{u}(\omega)\big)^2\Big\}.$$

The solution to above minimization problem for 2-D case has been provided and proven in [44]. We can easily extend the result to 3-D setting as follows

$$\boldsymbol{p}^*(\omega) = \begin{cases} 0, & \|\nabla\hat{u}(\omega)\|^2 \leq \dfrac{2\alpha}{\beta}; \\ \nabla\hat{u}(\omega), & \text{otherwise.} \end{cases} \tag{18}$$

The proof for the 3-D minimization is provided in Appendix.

D. Multi-resolution Algorithm

We apply a multi-resolution algorithm [28] that starts by estimating a coarse resolution image, expands it by interpolation and uses the result as an initialization for the next resolution layer. In this way, it requires few iterations at each resolution in the computation.

We summarize our algorithm as follows

1. **Input:** The input to the algorithm is an image v and parameters α, μ, τ, β_0, β_{max} and κ.
2. **Initialization:** Set $k = l$, i.e., start at the coarsest resolution layer and set the initial condition $\hat{u} = \hat{v}_l$, where $\hat{v}_l$ is obtained by down scaling $\hat{v}$ with ratio $1 : 2^l$, and $\hat{f} = 0$.
3. **Main Loop:** For the kth resolution layer, set $\beta = \beta_0$
   Repeat
   ① With $\hat{u}_k^{(i)}$, solve for $\hat{f}_k^{(i)}$ from Eq. (16);
   ② With $\hat{u}_k^{(i)}$, solve for $\boldsymbol{p}_k^{(i)}$ from Eq. (18);
   ③ With $\hat{f}_k^{(i)}$ and $\boldsymbol{p}_k^{(i)}$, solve for $\hat{u}_k^{(i+1)}$ from Eq. (12);
   ④ $\beta \leftarrow \kappa\beta$, $i \leftarrow i + 1$;
   until $\beta \geq \beta_{max}$
4. **Update the next resolution layer:** If $k > 1$, the result $\hat{u}_k$ and $\hat{f}_k$ is up scaled (2:1 ratio) by voxel replication as the initialization for the next resolution layer. The resolution layer is updated by $k = k-1$, and the algorithm proceeds by going again to Step 3. If $k = 1$, the result $\hat{u}_1$ and $\hat{f}_1$ are the final outputs of the algorithm.

E. Comparison with Other Variational Methods

We discuss the connection of the proposed HoL0MS with the other two variational methods for intensity inhomogeneity correction, i.e., TVH1 model [29] and HoTVL1 [37], both of which were proposed for Retinex problem. Based on the same image decomposition model (2), the two models are given as

- **TVH1 model:** uses TV norm and H^1 norm to regularize on $\hat{u}$ and $\hat{f}$ as follows

$$\min_{\hat{u}\geq 0, \hat{f}\geq 0} \quad \frac{1}{2}\int_\Omega (\hat{v} - \hat{u} - \hat{f})^2 dx + \alpha\int_\Omega |\nabla\hat{u}| dx + \frac{\mu}{2}\int_\Omega |\nabla\hat{f}|^2 dx + \frac{\tau}{2}\int_\Omega \hat{f}^2 dx,$$

  where the parameters are chosen as $\alpha = 1$, $\mu = 0.01$ and $\tau = 1.0 \times 10^{-3}$ in the tests.
- **HoTVL1 model:** employs the first and second order TV regularization on $\hat{u}$ and $\hat{f}$ as follows

$$\min_{\hat{u}\in\mathcal{B}_{\hat{u}}, \hat{f}\in\mathcal{B}_{\hat{f}}} \quad \frac{1}{2}\int_\Omega (\hat{v} - \hat{u} - \hat{f})^2 dx + \alpha\Big(\int_\Omega |\nabla\hat{u}| dx + \mu\int_\Omega |\nabla^2\hat{f}| dx\Big) + \frac{\tau}{2}\int_\Omega \hat{f}^2 dx,$$

  where the parameters are set to $\alpha = 10$, $\mu = 50$, $\tau = 1.0 \times 10^{-3}$ and box constraints are $\mathcal{B}_{\hat{u}} = \big[0, \max\{\hat{v}\}\big]$ and $\mathcal{B}_{\hat{f}} = \big[-\max\{\hat{v}\}, 0\big]$ in the tests.

We evaluate the performance of the three variational methods on a phantom data and a rodent data, both of which were acquired on a Bruker 9.4 Tesla MR instrument. The imaging protocol was a TurboRare_T2 sequence with the slice thickness of 1 mm, and the pixel spacing of 0.12 mm $\times$ 0.12 mm $\times$ 1 mm and 0.09 mm $\times$ 0.0.09 mm $\times$ 1 mm for phantom data and rodent data, respectively. One slice of the test images are displayed in Fig. 2, both of which present significant intensity inhomogeneity. The parameters used in HoL0MS are $\alpha = 0.02$, $\mu = 0.01$, $\tau = 1.0 \times 10^{-3}$, $\beta_0 = 1.0 \times 10^{-3}$, $\beta_{max} = 1 \times 10^3$ and $\kappa = 1.2$. The stopping rule for TVH1 and HoTVL1 is either the relative error reaches 1.0×10^{-4} or the iteration reaches 5×10^3.

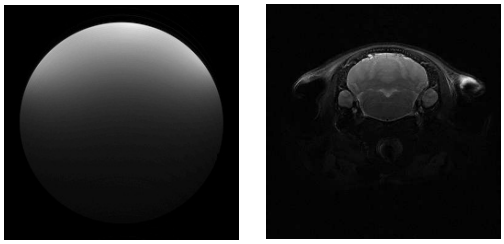

(a) (b)

Fig. 2. Two test images. (a) Phantom data and (b) Rodent data.

Fig. 3 and Fig. 4 display the visual comparison results of the phantom and rodent images, respectively. We can observe that HoL0MS produces the best visual results, whereas the bias corrected images are more homogeneous than TVH1 and HoTVL1. Indeed, as shown by Fig. 3 (a) and Fig. 4 (a), the solution of u from HoL0MS is able to give a piecewise constant approximation of the original image.

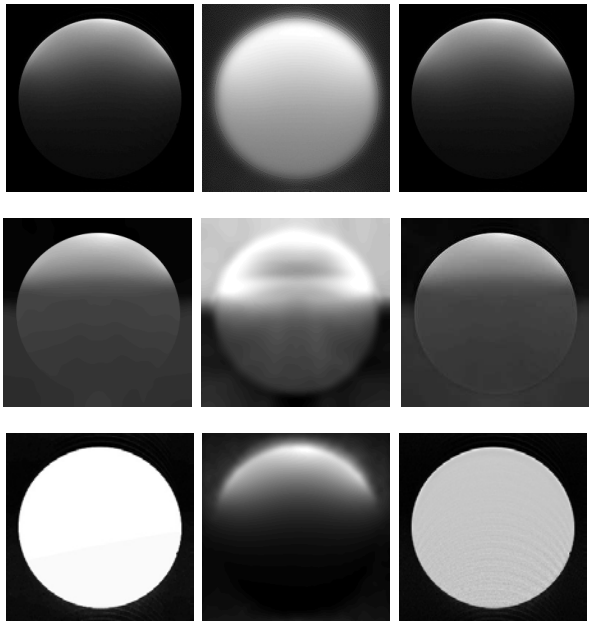

(a) (b) (c)

Fig. 3. Decomposition comparison of the phantom image among TVH1 (1st row), HoTVL1 (2nd row) and HoL0MS (3rd row). (a) u. (b) f. (c) v/f.

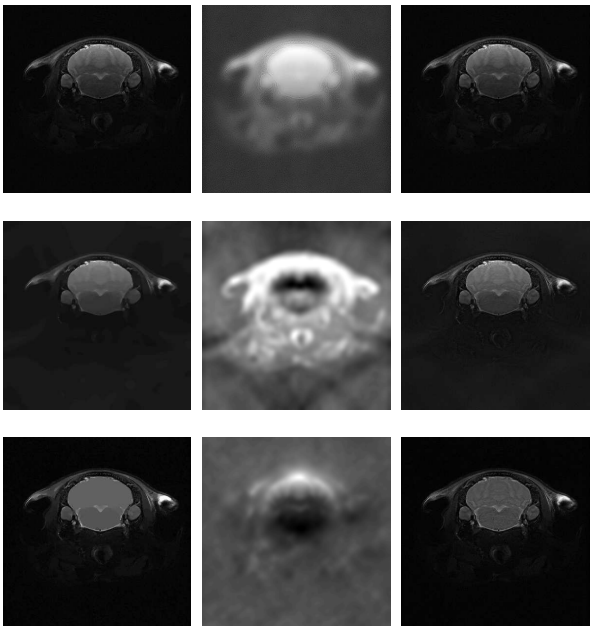

(a) (b) (c)

Fig. 4. Decomposition comparison of the rodent brain image among TVH1 (1st row), HoTVL1 (2nd row) and HoL0MS (3rd row). (a) u. (b) f. (c) v/f.

Relying on the comparison results, we can conclude on the three variational models for bias correction as follows

① From the perspective of bias correction, the second-order TV regularization outperforms the H^1 regularization in modeling the spatially smooth bias field function. It is partially because the high-order TV is contrast invariant. Thus, less edges and structures are contained in bias field.

② For the purpose of segmentation, the L_0 minimization on the gradient field works better than TV minimization. It is obviously that the L_0 regularization yields genuine piecewise-constant solution whereas TV does so only approximately. As shown in Fig. 4 (a), the solution of HoL0MS can identify the brain region from the non-brain region, which can be used as a guess for the brain mask.

V. Brain Extraction

As shown in the previous example, the solution u of our HoL0MS has already identified the brain region from the surrounding tissues. Therefore, we can use a simple thresholding technique to obtain the binary brain mask. More specifically, a three phase clustering method is used to classify the image domain into the brain region, the surrounding non-brain region, and the background outside the body. We adopt the k-means method [45] as an example for automatically computing the thresholds. As alternatives, fuzzy c-means method [46], Otsu's method [47] *etc.* can be implemented to perform a global clustering-based image thresholding.

Certain morphological operations are performed on the resultant brain mask, which have been widely used in brain extraction algorithms including 2-D PCNN [11], 3-D PCNN [12] and RATS [14] *etc.*. We use morphological erosion operation to remove the narrow bridges connecting continuous regions for isolation of the brain mask from adjacent structures. Then, we select the largest continuous component from the field of view by choosing the largest volume. After the brain mask is chosen, a morphological dilation operation is implemented to restore the size of the brain mask. For both morphological erosion and dilation, we use the same neighborhood with a radius r. In the end, we fill the holes to create a full 3-D geometry representation of the cropped brain.

VI. Validation and Discussion

In this section, we conduct a series of numerical experiments to validate the performance of our HoL0MS model. Both the HoL0MS model and 3-D PCNN are implemented Matlab on a MacBook Pro with Processor 2.2 GHz Intel Core i7. All the brain software including ANTs, FSL and BrainSuite are run on Linux Debian Jessie computer system. In the implementation, we simplify the Hessian operator H with the elements on the diagonal to reduce the computational costs.

A. Data

*Data Set 1: 4.7 T anatomy data set (*30 *volumes)*
The data set was used in [11]. All data volumes were obtained in a Bruker Biospec 4.7 T, 40 cm horizonal magnet. The imaging protocol was a RARE pulse sequence with slice thickness 1.2 mm and resolution $256 \times 256 \times 12$. The pixel spacing is 0.12 mm $\times$ 0.12 mm $\times$ 1.2 mm.

*Data Set 2: 17.6 T mouse data set (*12 *volumes)*
The data set was C57BL/6J adult mouse brains imaged in vivo on a 17.6 Tesla MR instrument at an isotropic spatial resolution of 0.1 mm and the resolution of $192\times96\times256$. The mouse brains were segmented into 20 anatomical structures [48], [49]. Both the MR images and atlas images can be download from http://brainatlas.mbi.ufl.edu/Database/dbdownload/.

Data Set 3: 9.4 T anatomy data set (8 volumes)
The data set was acquired in a Bruker 9.4 Tesla MR instrument. The imaging protocol was a TurboRare_T2 sequence with slice thickness 1 mm and resolution $384 \times 384 \times 24$. The pixel spacing is 0.09 mm $\times$ 0.09 mm $\times$ 1 mm.

For the purpose of numerical evaluation, it requires the manual masks for all images. There are publicly available ground truth for both *Data Set 1* and *Data Set 2*. For *Data Set 3*, we employed experienced technician manually created the masks served as the 'gold' standard.

B. Parameters Employed

The parameters for HoL0MS are described in TABLE I. We can fix most parameters in the evaluation, i.e., τ, β_0, κ, β_{max} and l. The piecewise constant parameter α and the radius for the morphological operator r vary with data sets. The smooth parameter μ is chosen as $\mu = 0.01$ for all rodent images and $\mu = 100$ for all human images.

TABLE I
THE VALUES OF THE COEFFICIENTS USED IN THE HOL0MS MODEL.

parameter	value	interpretation
α	0.01-0.1	piecewise constant parameter
μ	0.01	smooth parameter
τ	1.0×10^{-3}	boundedness control parameter
β_0	1.0×10^{-3}	initial value of β
β_{max}	1.0×10^{3}	maximum value of β
κ	1.2	update speed of β
l	3	number of layers in Algorithm
r	0.0-5.0	radius of morphological operator

C. Evaluation Methods

We use the coefficient of variations (CV) [50] to quantify the degree of intensity inhomogeneity, which is defined as

$$\mathrm{CV(T)} = \frac{\sigma(\mathrm{T})}{\mu(\mathrm{T})}, \tag{19}$$

where $\sigma(\mathrm{T})$ and $\mu(\mathrm{T})$ are the standard deviation and the mean of the intensities in the tissue T.

As shown in TABLE II, we use a number of metrics [51], i.e., true positive rate (TPR), false positive rate (FPR), volume overlap (VO), volume difference (VD) and average symmetric surface distance (SD), to measure the similarity of the brain masks obtained from automatic methods (Seg) to the manual standard (GT) .

D. Comparison with Established Brain Software

In this subsection, we compare the performance of HoL0MS with other well-known brain software. The comparison is conducted from two aspects: 1) comparing the results of inhomogeneity correction with N3 algorithm [16] and N4 algorithm [17]; 2) comparing the results of brain extraction with BET [4], BSE [52] and 3-D PCNN [12]. We list the implementation details of each software as follows

- **N3:** It is performed using Advanced Normalization Tools (ANTs). The parameters are shrink factor=4; number of iterations=50; and number of fitting levels=4.

TABLE II
THE EVALUATION METRICS.

Name	Definition	Unit	Best	Worst
TPR	$\frac{TP}{TP+FN}$	%	100	0
FPR	$\frac{FP}{FP+TN}$	%	0	100
VO	$\frac{Vol(Seg \cap GT)}{Vol(Seg \cup GT)}$	%	100	0
VD	$\frac{\lvert Vol(Seg) - Vol(GT)\rvert}{Vol(GT)}$	%	0	$< \infty$
SD	$\frac{\sum_{v \in \mathcal{B}_1} \min_{u \in \mathcal{B}_2} d(u,v) + \sum_{v \in \mathcal{B}_2} \min_{u \in \mathcal{B}_1} d(u,v)}{card(Seg \cup GT)}$	mm	0	$< \infty$

In the table, TP is true positives; TN is true negatives; FP is false positives; FN is false negatives; $\mathcal{B}_1$ and $\mathcal{B}_2$ in SD denote the boundary of Seg and GT, respectively.

- **N4:** It is performed N4 using Advanced Normalization Tools (ANTs). The parameters are kernel fwhm=0.15; Wiener filter noise=0.1; number of iterations=50; and fitting levels=4
- **BET:** We use FSL version 5.0 [53], [54] with parameter r=8 mm. All input images for BET are rescaled by a factor of 10 for better segmentation [11], [55].
- **BSE:** We use the BrainSuite 16a1 with iterations=3 [5], which is downloaded from http://brainsuite.org/.
- **3-D PCNN:** It can be downloaded from http://www.sbic.astar.edu.sg/research/lmi/PCNN3D%20binary.zip, where the radius of structural element is set to $p = 4$.

Firstly, the HoL0MS is tested on *Data Set 1*. The parameter α and r are defined as $\alpha = 0.01$ and $r = 0$. In order to evaluate the performance of bias correction, we manually labeled both gray matter and white matter, one slice of which are shown in Fig. 5. The CV on gray matter and white matter are calculated and compare with N3 and N4 in Fig. 6. It can be observed that the bias correction of HoL0MS is better than N4, which is better than N3 for both GM and WM.

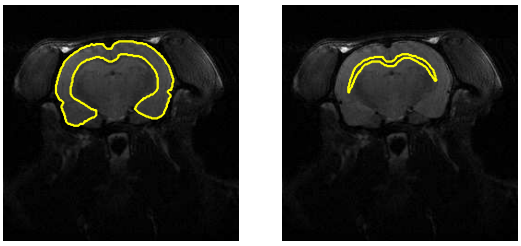

(a) Gray Matter (b) White Matter

Fig. 5. Manual labeled gray matter and white matter for *Data Set 1*. (a) Gray Matter and (b) White Matter.

We use the bias corrected images obtained from N4 as the input of BET, BSE and 3-D PCNN for brain extraction comparison. Fig. 7 shows examples of the brain boundaries identified by these methods on three slices of a 3-D volume, and TABLE III presents the quantitative results, i.e., TPR, FPR, VO, VD and SD, for different brain extraction algorithms. The p-values of two-sample single-tailed t-test between the proposed HoL0MS model and other methods are provided below each quantitative result. Generally speaking, the improvement of HoL0MS is statistically significant with

This article has been accepted for publication in a future issue of this journal, but has not been fully edited. Content may change prior to final publication. Citation information: DOI 10.1109/TMI.2016.2636026, IEEE Transactions on Medical Imaging

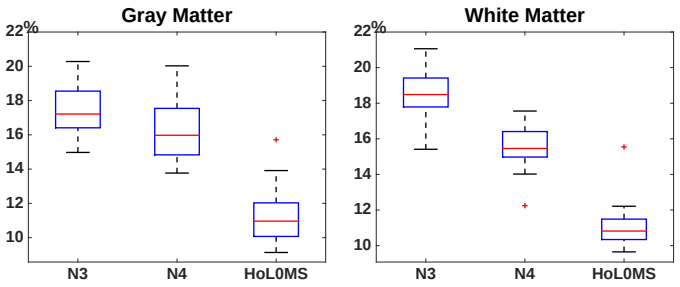

(a) (b)

Fig. 6. Comparison of accuracy of bias correction in terms of CV for *Data Set 1*. (a) CV of gray matter and (b) CV of white matter.

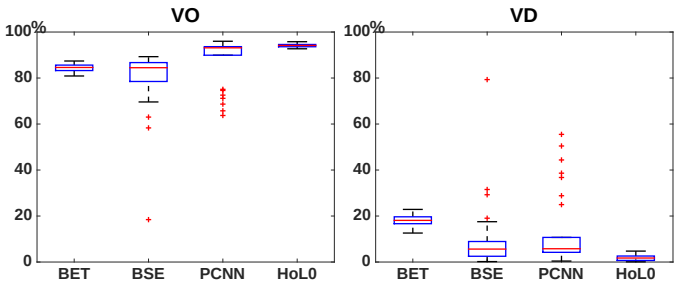

Fig. 8. Comparison of accuracy of various automatic methods for *Data Set 1* in terms of VO and VD.

$p < 0.05$ except for TPR, where the BET gives the best. However, BET over-segments the brain region with a much bigger FPR than HoL0MS. According to both visual results and the quantitative metrics, our HoL0MS model outperforms the rest of competing methods. Furthermore, we can make the following conclusions based on the experiments of *Data Set 1*:

① BET tends to over-segment the brain mask for rodent images;
② BSE only performs good for the middle part of brain and is less accurate in both anterior and posterior brain;
③ 3-D PCNN may over-segment the brain mask due to the low contrast on the boundary;
④ HoL0MS can well segment the brain mask even when the radius for the morphological operator is set to $r = 0$. It is mainly because the piecewise constant solution u can successfully identify the brain region from the non-brain region.

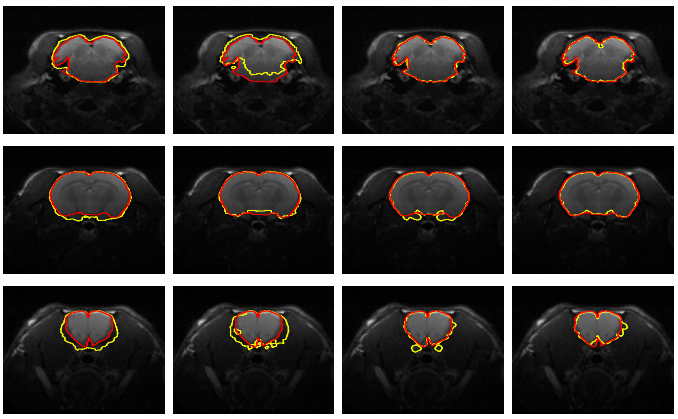

(a) BET (b) BSE (c) 3-D PCNN (d) HoL0MS

Fig. 7. Comparison of brain masks (axial view) obtained using automatic methods on selected slices of a mouse volume from *Data Set 1*, where red curves denote the manual gold standard and yellow curves denote the automatic method. (a) BET; (b) BSE; (c)3-D PCNN and (d) HoL0MS.

Secondly, the HoL0MS model is tested on *Data Set 2*. The values of α and r are given as $\alpha = 0.1$ and $r = 5$. Since the atlas of all the 12 volumes are available publicly, as displayed in Fig. 9, we compute the CV on each structure and compare them with both N3 and N4 in Fig. 10. It is clearly shown that the bias correction of HoL0MS is better than both N3 and N4 for all brain structures. More importantly, the bias correction of HoL0MS is much better than N4 on brain stem, olfactory bulb, cerebellum *etc.*, where the intensity inhomogeneity is most serious.

Fig. 9. Atlas surface rendering and cutting plane display of the atlas for one volume from *Data Set 2*. There are total 20 structures including neocortex, hippocampus, amygdala, olfactory bulbs, basal forebrain and septum, caudate-putamen, globus pallidus, thalamus, hypothalamus, central gray, superior colliculi, inferior colliculi, the rest of midbrain, cerebellum, brainstem, corpus, callosum/external capsule, internal capsule, anterior commissure, fimbria and ventricles.

When conducting the experiments on brain extraction, we use different input for brain extraction algorithms, i.e., the original image, N4 corrected image and HoL0MS corrected image. We display the quantitative metrics in TABLE IV. No matter which brain extraction method has been used, most metrics obtained based on the HoL0MS corrected image give the best mean and standard deviation. In TABLE IV, the p-values between the proposed HoL0MS model and other methods are evaluated and indicated by * for those quantitative results with $p < 0.05$. It is shown that the improvement of the proposed HoL0MS is statistically significant compared to BET, BSE and 3-D PCNN with original image and N4 corrected image. Moreover, the box plots of VO and SD are presented in Fig. 11. We can observe, for 3-D PCNN, there is significant improvement of the segmentation accuracy based on HoL0MS corrected image compared to N4 corrected image, the accuracy of which is also improved compared to the original image. In fact, TABLE IV shows that the quantitative metrics of 3-D PCNN based on HoL0MS corrected image are similar to the ones obtained by our HoL0MS method, both of which are better than BET and BSE.

Furthermore, two typical results are displayed in Fig. 12. It can be observed that BET can well segment the central region of brain, but performs poorly on the anterior and posterior brain for all input images. The segmentation results of BSE vary with the original image, and the influence of bias correction seems limited. For 3-D PCNN, the best brain boundaries are obtained using the HoL0MS corrected image,

TABLE III
MEAN AND STANDARD DEVIATION OF QUANTITATIVE RESULTS FOR *Data Set 1* WITH DIFFERENT BRAIN EXTRACTION METHODS. BEST PERFORMANCE BASED ON MEAN IS INDICATED BY BOLD FONT.

Method	TPR (%)	FPR (%)	VO (%)	VD (%)	SD (mm)
BET	$\mathbf{99.82 \pm 0.27}$ (7.3e-16)	2.42 ± 0.25 (5.3e-43)	84.46 ± 1.70 (2.9e-36)	18.05 ± 2.37 (3.0e-39)	5.65 ± 0.76 (9.7e-35)
BSE	86.90 ± 15.76 (2.4e-04)	1.18 ± 0.39 (2.2e-13)	79.61 ± 13.81 (1.7e-07)	10.10 ± 15.14 (2.1e-03)	7.66 ± 8.85 (1.5e-04)
3-D PCNN	98.89 ± 0.76 (5.7e-07)	1.88 ± 2.09 (2.8e-04)	87.94 ± 10.21 (7.8e-04)	13.15 ± 15.99 (1.5e-04)	6.07 ± 8.34 (1.8e-03)
HoL0MS	97.56 ± 1.11 (NA)	$\mathbf{0.48 \pm 0.13}$ (NA)	$\mathbf{94.14 \pm 0.72}$ (NA)	$\mathbf{1.90 \pm 1.32}$ (NA)	$\mathbf{1.44 \pm 0.39}$ (NA)

which can help 3-D PCNN to successfully locate the brain stem from other tissues. As shown, our HoL0MS is also proved to be able to produce satisfactory brain masks, where the segmented brain masks are quite close to the manually labeled ones. In Fig. 13, we display the 3D renderings of the brain masks of the same volumes for visual comparison, where the brain masks of BSE, BET and 3-D PCNN are obtained on HoL0MS corrected image. Obviously, both 3-D PCNN and our HoL0MS give the satisfactory 3-D brain mask.

We can make the following summary on the experiments on *Data Set 2*:

① Both BET and BSE are somehow robust against intensity inhomogeneity. Therefore, the accuracy of brain extraction is improved limited by applying an efficient bias correction method to the test images;

② 3-D PCNN is sensitive to intensity inhomogeneity. Thus, the bias corrected image of high quality can improve its segmentation results significantly.

Lastly, we test the HoL0MS on *Data Set 3*. We set $\alpha = 0.02$ and $r = 1$ for HoL0MS. We display the segmentation results in Fig. 14 and the quantitative metrics in TABLE V. Similarly, the p-values between the proposed HoL0MS model and other methods are evaluated and indicated by * for those quantitative results with $p < 0.05$. It is shown that both visual results and the quantitative results are consistent with our conclusion on *Data Set 2*. We observe that BET, BSE and 3-D PCNN with HoL0MS corrected images give better brain extraction results than N4 corrected images. Indeed, the four slices in Fig. 14 show that 3-D PCNN based on HoL0MS corrected images overtakes the segmentation results of HoL0MS, the boundaries of which are the closest one to the manually labeled mask. Meanwhile, the HoL0MS method still gives the best overall performance as shown by TABLE V and Fig. 15, which shows that HoL0MS is more robust to the diversity of brain shapes and image qualities, *etc.*.

E. Computational Complexity and Efficiency

In this subsection, we analyze the computational cost of HoL0MS. The computational complexity of HoL0MS is about $O(n(17MNL+4MNL\log(MNL)))$, where n is the number of iterations to satisfy the stopping condition.

We display the computational time of 3-D PCNN and HoL0MS for the three data sets in TABLE VI. We see that the 3-D PCNN algorithm need more than 16 minutes to segment one volume in *Data Set 2*, while our HoL0MS only need less than 4 minutes without any other optimization technique such as GPU and multi-core programming. Moreover, 3-D PCNN requires an additional step for bias correction. Therefore, both complexity and numerical experiments demonstrate that our HoL0MS is highly efficient and scalable.

TABLE VI
THE CPU TIME OF 3-D PCNN AND HOL0MS MODEL IN SECONDS.

	Data Set 1	Data Set 2	Data Set 3
$M \times N \times L$	$256 \times 256 \times 12$	$192 \times 96 \times 256$	$384 \times 384 \times 24$
3-D PCNN	46.32	971.24	167.54
HoL0MS	31.71	213.23	166.74

F. Experiments on Human Brain Extraction and Limitations

Although our discussion focuses on rodent images, the HoL0MS is also suitable for human brain extraction. We downloaded a T2-weighted data set from http://insight-journal.org/midas/collection/view/190. There are total five images acquired using a 3T GE at BWH in Boston, MA. We set $\alpha = 0.02$ and $r = 5$ for all images and tabulate the quantitative metrics in TABLE VII. As shown, HoL0MS gives relatively high values of TPR, VO and low values of FPR, VD and SD. Besides, we use *data 5* as an example and present selective 2-D and 3-D segmentation results in Fig. 16 and Fig. 17, respectively. It is obviously shown that our HoL0MS method works well for human brain extraction.

TABLE VII
BRAIN EXTRACTION OF HOL0MS METHOD FOR HUMAN 3T IMAGES.

Data	TPR	FPR	VO	VD	HD
1	92.76	0.0045	92.73	7.22	0.1314
2	94.25	0.0558	93.87	5.36	0.1152
3	95.45	0.0626	95.14	4.22	0.0884
4	94.34	0.3088	92.67	3.86	0.1487
5	96.89	0.0391	96.64	2.85	0.0695

However, similar to 3-D PCNN, the HoL0MS has its limitation in processing the T1-weighted MR images due to the low contrast between the skull and the cerebrospinal (CFS). In fact, we are still able to use HoL0MS to remove the severe intensity inhomogeneity for T1-weighted images and images of other modalities. Here, we use a 7T

TABLE IV
MEAN AND STANDARD DEVIATION OF QUANTITATIVE RESULTS FOR *Data Set 2* WITH DIFFERENT BRAIN EXTRACTION METHODS. BEST PERFORMANCE BASED ON MEAN IS INDICATED BY BOLD FONT.

Method	Data	TPR	FPR	VO	VD	SD
BET	Orig	95.33 ± 0.92	$4.94 \pm 2.05^*$	$68.21 \pm 7.87^*$	$36.92 \pm 17.36^*$	$57.80 \pm 14.56^*$
	N4	$94.76 \pm 0.86^*$	$3.36 \pm 1.51^*$	$74.49 \pm 6.74^*$	$23.05 \pm 13.37^*$	$47.30 \pm 11.28^*$
	HoL0	$95.07 \pm 0.72^*$	$3.02 \pm 0.54^*$	$75.89 \pm 2.89^*$	$20.53 \pm 5.50^*$	$44.78 \pm 5.52^*$
BSE	Orig	93.16 ± 6.67	$3.27 \pm 5.11^*$	$78.14 \pm 17.09^*$	$26.59 \pm 40.58^*$	$50.25 \pm 51.33^*$
	N4	$92.32 \pm 6.77^*$	1.69 ± 3.61	$83.71 \pm 12.21^*$	14.13 ± 28.47	$33.83 \pm 35.10^*$
	HoL0	$91.87 \pm 6.24^*$	1.61 ± 3.35	$83.44 \pm 11.89^*$	13.92 ± 27.11	$36.18 \pm 40.60^*$
3-D PCNN	Orig	$93.54 \pm 4.47^*$	$1.51 \pm 1.55^*$	$83.55 \pm 6.79^*$	$13.99 \pm 10.67^*$	$40.08 \pm 20.14^*$
	N4	94.79 ± 2.30	$1.12 \pm 1.25^*$	$87.19 \pm 6.37^*$	$9.47 \pm 8.83^*$	$28.94 \pm 17.80^*$
	HoL0	$\mathbf{96.82 \pm 1.37^*}$	0.61 ± 0.27	92.15 ± 1.16	$2.85 \pm 2.74^*$	$\mathbf{13.97 \pm 2.22}$
HoL0MS		95.79 ± 1.12	$\mathbf{0.47 \pm 0.0009}$	$\mathbf{92.19 \pm 0.88}$	$\mathbf{1.37 \pm 0.96}$	14.56 ± 2.45

* indicates $p < 0.05$ by single-tailed t-test between the HoL0MS method and other methods.

TABLE V
MEAN AND STANDARD DEVIATION OF QUANTITATIVE RESULTS FOR *Data Set 3* WITH DIFFERENT BRAIN EXTRACTION METHODS. BEST PERFORMANCE BASED ON MEAN IS INDICATED BY BOLD FONT.

Method	Data	TPR	FPR	VO	VD	SD
BET	Orig	$88.84 \pm 1.77^*$	$0.80 \pm 0.03^*$	$80.32 \pm 1.16^*$	$2.05 \pm 1.26^*$	$11.97 \pm 0.77^*$
	N4	$90.93 \pm 1.81^*$	$0.77 \pm 0.04^*$	$82.54 \pm 1.12^*$	$2.46 \pm 1.28^*$	$10.70 \pm 0.81^*$
	HoL0	$93.84 \pm 1.33^*$	$0.74 \pm 0.06^*$	$85.51 \pm 0.69^*$	$3.58 \pm 2.37^*$	$10.70 \pm 1.19^*$
BSE	Orig	$89.48 \pm 9.14^*$	$1.32 \pm 0.89^*$	$76.52 \pm 7.67^*$	$13.54 \pm 13.04^*$	$18.24 \pm 14.83^*$
	N4	$90.86 \pm 9.09^*$	$1.24 \pm 1.12^*$	$78.80 \pm 9.62^*$	$12.51 \pm 15.86^*$	$18.65 \pm 21.03^*$
	HoL0	97.00 ± 2.16	$1.63 \pm 1.95^*$	$81.95 \pm 11.38^*$	$18.38 \pm 26.09^*$	$14.38 \pm 14.53^*$
3-D PCNN	Orig	$87.04 \pm 6.97^*$	$0.82 \pm 0.79^*$	$78.88 \pm 4.71^*$	$13.89 \pm 7.15^*$	$20.32 \pm 9.87^*$
	N4	96.52 ± 2.20	$1.26 \pm 0.95^*$	$83.34 \pm 8.21^*$	$15.82 \pm 11.66^*$	$20.05 \pm 13.47^*$
	HoL0	$\mathbf{98.82 \pm 0.93}^*$	$0.59 \pm 0.48^*$	92.01 ± 4.40	$6.62 \pm 6.80^*$	6.19 ± 5.61
HoL0MS		96.85 ± 0.38	$\mathbf{0.27 \pm 0.08}$	$\mathbf{93.54 \pm 1.20}$	$\mathbf{0.93 \pm 0.70}$	$\mathbf{3.24 \pm 1.37}$

* indicates $p < 0.05$ by single-tailed t-test between the HoL0MS method and other methods.

human T1 MR scan as an example, which is downloaded from http://multimodal.projects.nitrc.org/MMRR-3T7T-2-1_multimodal.tar.gz (posted by Bennett Landman). As shown in Fig. 18, obvious intensity inhomogeneity are presented in the axial, sagittal and coronal direction of the image. By applying HoL0MS for bias correction, we can recover the brain region with high visual quality.

VII. CONCLUSION

In this paper, we introduced a high-order variational model for bias correction and considered its applications in brain extraction. We formulated the minimization problem using an L_0 minimization and a high-order smooth regularization in the gradient field. The existence of the solution was derived in the work. We used a fast multi-resolution solution to the corresponding variational problem, resulting in an efficient algorithm. The HoL0MS model was tested on rodent brain volumes from three different acquisition configurations and quantitatively compared against the well-known brain software for both bias correction and rodent brain extraction. Applications to human brain MR images were also discussed and presented. The numerical results demonstrate that HoL0MS can be used as a powerful tool for intensity inhomogeneity correction and brain extraction. The extracted brain images with bias correction can facilitate other image processing tasks such as brain registration, segmentation *etc.*.

APPENDIX

We consider the minimum of the following problem

$$E = \frac{2\alpha}{\beta}\mathcal{C}\big(\boldsymbol{p}(\omega)\big) + \big(\boldsymbol{p}(\omega) - \nabla\hat{u}(\omega)\big)^2. \tag{20}$$

Proof. Followed [44], we discuss the minimizer E^* in two cases as follows.

① When $\frac{2\alpha}{\beta} \geq \|\nabla\hat{u}(\omega)\|^2$ and $\boldsymbol{p}(\omega) \neq 0$, Eq. (20) yields

$$\begin{aligned} E(\boldsymbol{p}(\omega)) =& \big(p_1(\omega) - \partial_x\hat{u}(\omega)\big)^2 + \big(p_2(\omega) - \partial_y\hat{u}(\omega)\big)^2 \\ &+ \big(p_3(\omega) - \partial_z\hat{u}(\omega)\big)^2 + \frac{2\alpha}{\beta} \\ &\geq \frac{2\alpha}{\beta} \geq \|\nabla\hat{u}(\omega)\|^2. \end{aligned} \tag{21}$$

If $\boldsymbol{p}(\omega) = 0$, Eq. (20) leads to

$$E(\boldsymbol{p}(\omega)) = (\partial_x\hat{u}(\omega))^2 + (\partial_y\hat{u}(\omega))^2 + (\partial_z\hat{u}(\omega))^2. \tag{22}$$

Thus, the minimum E^* is obtained when $\boldsymbol{p}(\omega) = 0$.

② When $\|\nabla\hat{u}(\omega)\|^2 > \frac{2\alpha}{\beta}$ and $\boldsymbol{p}(\omega) = 0$, Eq. (22) still holds. If $\boldsymbol{p}(\omega) \neq 0$, Eq. (21) reaches its minimum when $\boldsymbol{p}(\omega) = \nabla\hat{u}(\omega)$. Comparing these two values, the minimum E^* is obtained when $\boldsymbol{p}(\omega) = \nabla\hat{u}(\omega)$. ■

ACKNOWLEDGMENT

We would like to thank the authors of [29] and [37] for sharing their source codes, and the reviewers of this manuscript for their helpful comments and suggestions. The work is partially supported by research grants 1334K00084

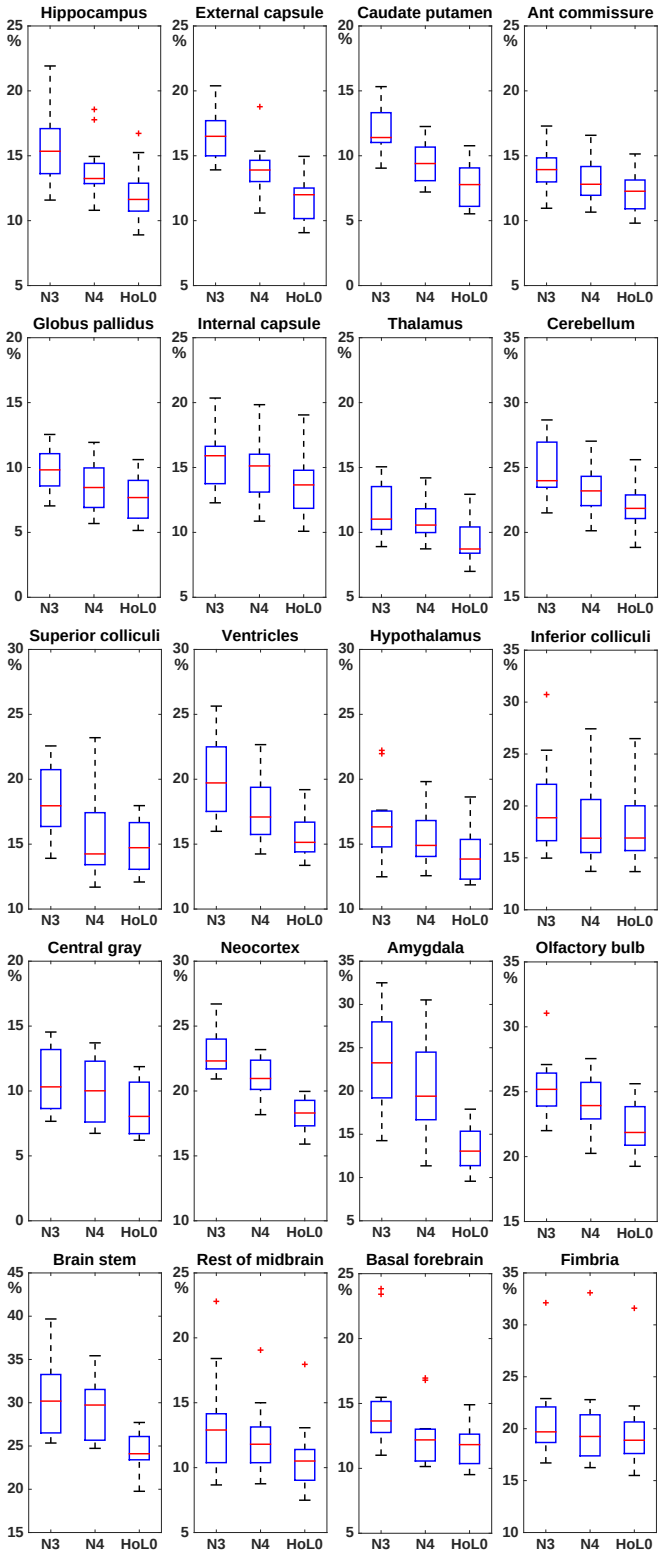

Fig. 10. Comparison of accuracy of bias correction in terms of CV for *Data Set 2*.

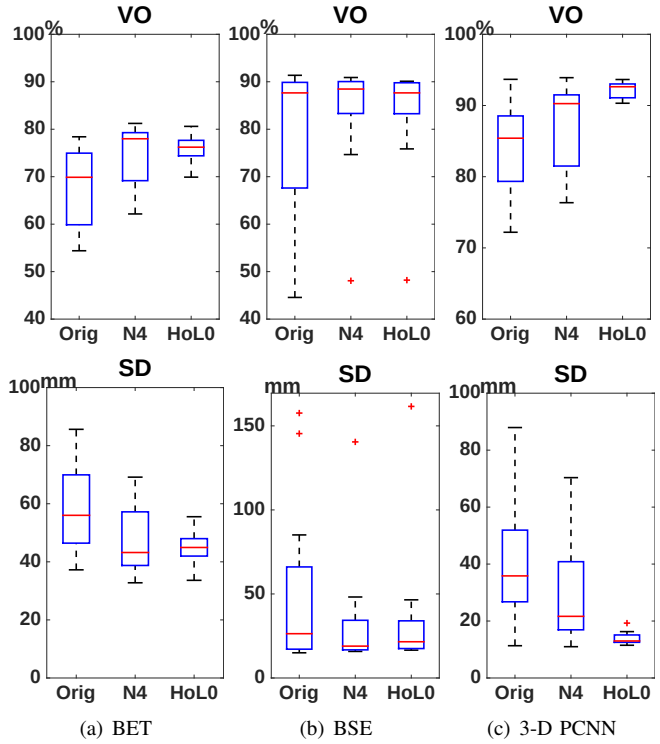

Fig. 11. Comparison of the accuracy of brain extraction based on different bias correction approaches in terms of VO and SD for *Data Set 2*. (a) BET (b) BSE and (c) 3-D PCNN.

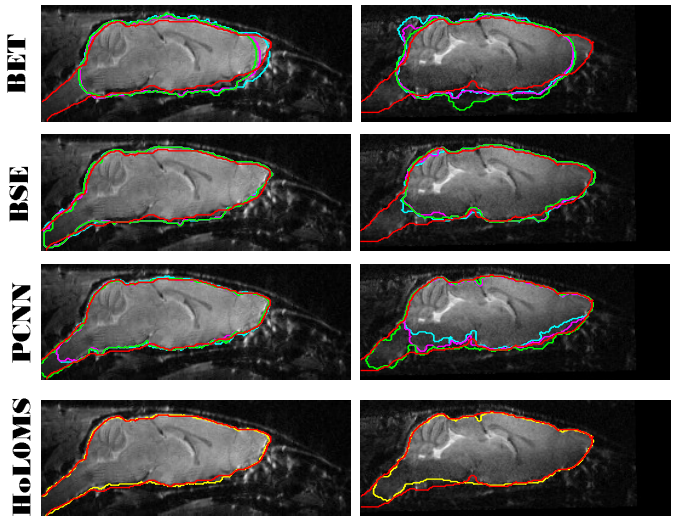

Fig. 12. Comparison of brain masks (sagittal view) obtained using automatic methods on selected slices of one mouse brain from *Data Set 2*, where red curves represent the manual gold standard, cyan curves represent the brain mask obtained using the original image, magenta curves represents the brain mask obtained using N4 corrected image, green curves represent the brain mask using HoL0MS corrected image and yellow curves represent the boundaries obtained by HoL0MS.

from JCO A*STAR, Singapore. Dr. Yuping Duan is supported by the Ministry of Science and Technology of China ("863" Program: 2015AA020101), and NSFC 11526208. Dr. Huibin Chang is supported by NSFC 11426165 and 11501413, Tianjin 131 Talent Project and China Scholarship Council (CSC). Dr. Chunlin Wu is supported by NSFC 11301289.

REFERENCES

[1] O. Natt, T. Watanabe, S. Boretius, J. Radulovic, J. Frahm, and T. Michaelis, "High-resolution 3d mri of mouse brain reveals small cerebral structures in vivo," *Journal of Nuroscience Methods*, vol. 120, no. 2, pp. 203–209, 2002.

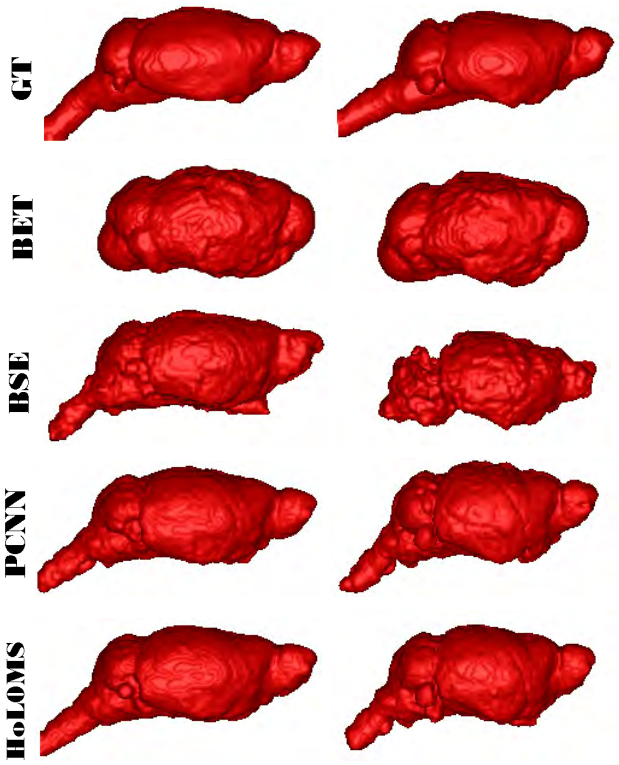

Fig. 13. 3-D brain segmentation of a mouse image from *Data Set 2*.

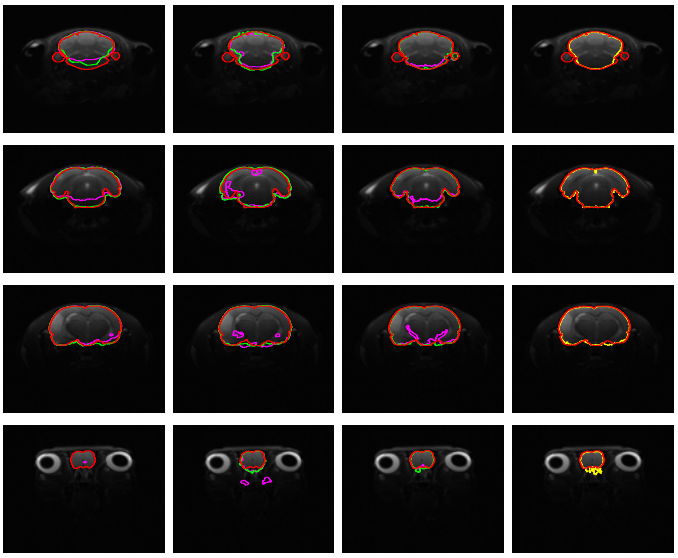

(a) BET (b) BSE (c) 3-D PCNN (d) HoL0MS

Fig. 14. Comparison of brain masks (axial view) obtained using automatic methods on selected slices of one rat brain from *Data Set 3*, where red curves represent the manual gold standard, magenta curves represents the brain mask obtained using N4 corrected image, green curves represent the brain mask using HoL0MS corrected image and yellow curves represent the boundaries obtained by HoL0MS. (a) BET; (b) BSE; (c) 3-D PCNN and (d) HoL0MS.

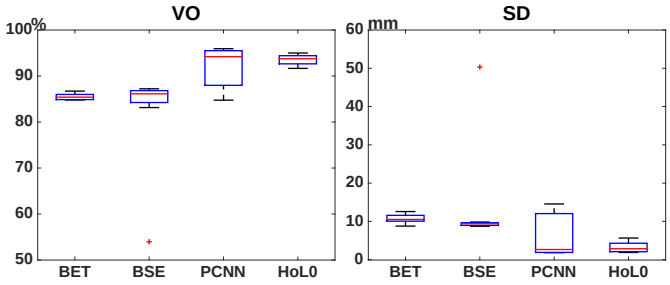

Fig. 15. Comparison of accuracy of various automatic methods for *Data Set 3* using VO and SD.

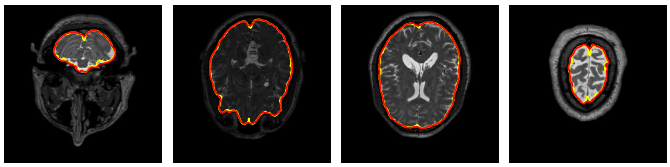

Fig. 16. Selective results of human brain extraction, where red curves denote the manual gold standard and yellow curves denote the HoL0MS model.

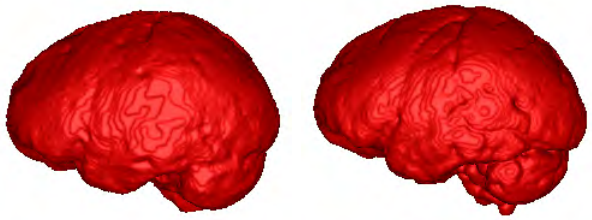

(a) Ground Truth (b) HoL0MS

Fig. 17. 3-D brain segmentation of a human 3T MR image. (a) Ground Truth and (b)HoL0MS.

by automated morphological analyses of magnetic resonance images," *Neuroimage*, vol. 49, no. 3, pp. 2340–2351, 2010.

[2] D. Van Dam and P. P. De Deyn, "Drug discovery in dementia: the role of rodent models," *Nature Reviews Drug Discovery*, vol. 5, no. 11, pp. 956–970, 2006.

[3] J. Zhang, Q. Peng, Q. Li, N. Jahanshad, Z. Hou, M. Jiang, N. Masuda, D. R. Langbehn, M. I. Miller, S. Mori *et al.*, "Longitudinal characterization of brain atrophy of a huntington's disease mouse model

[4] S. M. Smith, "Fast robust automated brain extraction," *Human Brain Mapping*, vol. 17, no. 3, pp. 143–155, 2002.

[5] D. W. Shattuck and R. M. Leahy, "Brainsuite: an automated cortical surface identification tool," *Medical Image Analysis*, vol. 6, no. 2, pp. 129–142, 2002.

[6] F. Ségonne, A. Dale, E. Busa, M. Glessner, D. Salat, H. Hahn, and B. Fischl, "A hybrid approach to the skull stripping problem in MRI," *Neuroimage*, vol. 22, no. 3, pp. 1060–1075, 2004.

[7] K. Van Leemput, F. Maes, D. Vandermeulen, and P. Suetens, "Automated model-based bias field correction of mr images of the brain," *IEEE Transactions on Medical Imaging*, vol. 18, no. 10, pp. 885–896, 1999.

[8] J. Lee, J. Jomier, S. Aylward, M. Tyszka, S. Moy, J. Lauder, and M. Styner, "Evaluation of atlas based mouse brain segmentation," *Proceedings of SPIE 7259, Medical Imaging 2009: Image Processing, 725943*, vol. 7259, pp. 725 943–725 949, 2009.

[9] I. Oguz, J. Lee, F. Budin, A. Rumple, M. Mcmurray, C. Ehlers, F. Crews, J. Johns, and M. Styner, "Automatic skull-stripping of rat MRI/DTI scans and atlas building." *Proceedings of SPIE 7962, Medical Imaging 2011: Image Processing, 796225*, vol. 7962, no. 4, pp. 7 962 251–7 962 257, 2011.

[10] M. G. Uberti, M. D. Boska, and Y. Liu, "A semi-automatic image segmentation method for extraction of brain volume from in vivo mouse head magnetic resonance imaging using constraint level sets," *Journal of Neuroscience Methods*, vol. 179, no. 2, pp. 338–344, 2009.

[11] M. Murugavel and J. M. Sullivan, "Automatic cropping of MRI rat brain volumes using pulse coupled neural networks," *Neuroimage*, vol. 45, no. 3, pp. 845–854, 2009.

[12] N. Chou, J. Wu, J. B. Bingren, A. Qiu, and K.-H. Chuang, "Robust automatic rodent brain extraction using 3-D pulse-coupled neural networks

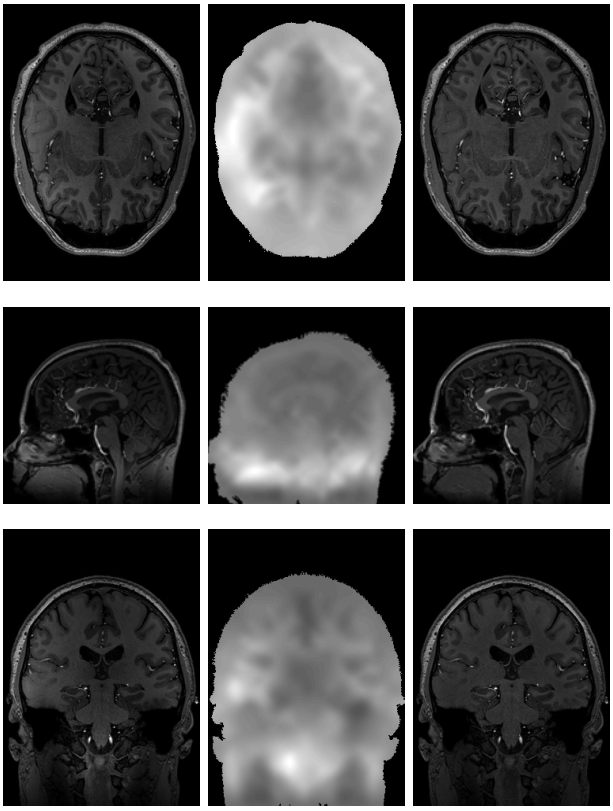

(g) Original image (h) Estimated bias (i) Corrected image

Fig. 18. Axial, sagittal and coronal view of Human 7T T1 MRI. (a) Original image; (b) Estimated bias field and (c) Corrected image.

(PCNN)," *IEEE Transactions on Image Processing*, vol. 20, no. 9, pp. 2554–2564, 2011.

[13] J. Li, X. Liu, J. Zhuo, R. P. Gullapalli, and J. M. Zara, "An automatic rat brain extraction method based on a deformable surface model," *Journal of Neuroscience Methods*, vol. 218, no. 1, pp. 72–82, 2013.

[14] I. Oguz, H. Zhang, A. Rumple, and M. Sonka, "Rats: rapid automatic tissue segmentation in rodent brain MRI," *Journal of Neuroscience Methods*, vol. 221, pp. 175–182, 2014.

[15] T. Truong, D. Chakeres, and P. Schmalbrock, "Effects of B0 and B1 inhomogeneity in ultra-high field mri," *Proc. Intl. Soc. Mag. Reson. Med*, vol. 11, pp. 2170–2170, 2004.

[16] J. G. Sled, A. P. Zijdenbos, and A. C. Evans, "A nonparametric method for automatic correction of intensity nonuniformity in mri data," *IEEE Transactions on Medical Imaging*, vol. 17, no. 1, pp. 87–97, 1998.

[17] N. J. Tustison, B. B. Avants, P. Cook, Y. Zheng, A. Egan, P. Yushkevich, J. C. Gee *et al.*, "N4itk: improved N3 bias correction," *IEEE Transactions on Medical Imaging*, vol. 29, no. 6, pp. 1310–1320, 2010.

[18] U. Vovk, F. Pernuš, and B. Likar, "A review of methods for correction of intensity inhomogeneity in MRI," *IEEE Transactions on Medical Imaging*, vol. 26, no. 3, pp. 405–421, 2007.

[19] M. N. Ahmed, S. M. Yamany, N. Mohamed, A. Farag, T. Moriarty *et al.*, "A modified fuzzy c-means algorithm for bias field estimation and segmentation of mri data," *IEEE Transactions on Medical Imaging*, vol. 21, no. 3, pp. 193–199, 2002.

[20] D. Mumford and J. Shah, "Optimal approximations by piecewise smooth functions and associated variational problems," *Communications on Pure and Applied Mathematics*, vol. 42, no. 5, pp. 577–685, 1989.

[21] T. F. Chan, L. Vese *et al.*, "Active contours without edges," *IEEE transactions on Image processing*, vol. 10, no. 2, pp. 266–277, 2001.

[22] C. Li, C.-Y. Kao, J. C. Gore, and Z. Ding, "Minimization of region-scalable fitting energy for image segmentation," *IEEE Transactions on Image Processing*, vol. 17, no. 10, pp. 1940–1949, 2008.

[23] C. Li, R. Huang, Z. Ding, C. Gatenby, D. Metaxas, and J. Gore, "A variational level set approach to segmentation and bias correction of images with intensity inhomogeneity," in *Medical Image Computing and Computer-Assisted Intervention*, 2008, pp. 1083–1091.

[24] C. Li, R. Huang, Z. Ding, J. Gatenby, D. N. Metaxas, and J. C. Gore, "A level set method for image segmentation in the presence of intensity inhomogeneities with application to MRI," *IEEE Transactions on Image Processing*, vol. 20, no. 7, pp. 2007–2016, 2011.

[25] F. Li, M. K. Ng, and C. Li, "Variational fuzzy Mumford-Shah model for image segmentation," *SIAM Journal on Applied Mathematics*, vol. 70, no. 7, pp. 2750–2770, 2010.

[26] E. H. Land and J. J. McCann, "Lightness and retinex theory," *JOSA*, vol. 61, no. 1, pp. 1–11, 1971.

[27] L. I. Rudin, S. Osher, and E. Fatemi, "Nonlinear total variation based noise removal algorithms," *Physica D: Nonlinear Phenomena*, vol. 60, no. 1, pp. 259–268, 1992.

[28] R. Kimmel, M. Elad, D. Shaked, R. Keshet, and I. Sobel, "A variational framework for retinex," *International Journal of Computer Vision*, vol. 52, no. 1, pp. 7–23, 2003.

[29] M. K. Ng and W. Wang, "A total variation model for retinex," *SIAM Journal on Imaging Sciences*, vol. 4, no. 1, pp. 345–365, 2011.

[30] W. Ma, J.-M. Morel, S. Osher, and A. Chien, "An L1-based variational model for retinex theory and its application to medical images," in *IEEE Conference on Computer Vision and Pattern Recognition (CVPR)*, 2011, pp. 153–160.

[31] W. Ma, S. Osher, and S. Esedoglu, "A TV Bregman iterative model of retinex theory." *Inverse Problems & Imaging*, vol. 6, no. 4, 2012.

[32] D. Zosso, G. Tran, and S. Osher, "A unifying retinex model based on non-local differential operators," in *Proceedings of SPIE 8657, Computational Imaging XI, 865702*, 2013, pp. 865 702–865 702.

[33] A. Chambolle and P.-L. Lions, "Image recovery via total variation minimization and related problems," *Numerische Mathematik*, vol. 76, no. 2, pp. 167–188, 1997.

[34] S. Setzer and G. Steidl, "Variational methods with higher order derivatives in image processing," *Approximation*, vol. 12, pp. 360–386, 2008.

[35] S. Setzer, G. Steidl, and T. Teuber, "Infimal convolution regularizations with discrete l1-type functionals," *Communications in Mathematical Sciences*, vol. 9, no. 3, pp. 797–872, 2011.

[36] K. Bredies, K. Kunisch, and T. Pock, "Total generalized variation," *SIAM Journal on Imaging Sciences*, vol. 3, no. 3, pp. 492–526, 2010.

[37] J. Liang and X. Zhang, "Retinex by higher order total variation L^1 decomposition," *Journal of Mathematical Imaging and Vision*, vol. 52, no. 3, pp. 345–355, 2015.

[38] Y. Duan, H. Chang, W. Huang, J. Zhou, Z. Lu, and C. Wu, "The regularized mumford–shah model for bias correction and segmentation of medical images," *IEEE Transactions on Image Processing*, vol. 24, no. 11, pp. 3927–3938, 2015.

[39] Y. Wang, J. Yang, W. Yin, and Y. Zhang, "A new alternating minimization algorithm for total variation image reconstruction," *SIAM Journal on Imaging Sciences*, vol. 1, no. 3, pp. 248–272, 2008.

[40] Z. Lu and Y. Zhang, "Sparse approximation via penalty decomposition methods," *SIAM Journal on Optimization*, vol. 23, no. 4, pp. 2448–2478, 2013.

[41] Y. Zhang, B. Dong, and Z. Lu, "L_0 minimization for wavelet frame based image restoration," *Mathematics of Computation*, vol. 82, no. 282, pp. 995–1015, 2013.

[42] M. Nikolova, "Description of the minimizers of least squares regularized with ℓ_0-norm. uniqueness of the global minimizer," *SIAM Journal on Imaging Sciences*, vol. 6, no. 2, pp. 904–937, 2013.

[43] R. Bracewell, "The Fourier Transform & its applications," *McGraw-Hill, New York*, 1965.

[44] L. Xu, C. Lu, Y. Xu, and J. Jia, "Image smoothing via L_0 gradient minimization," *ACM Transactions on Graphics*, vol. 30, no. 6, pp. 174:1–12, 2011.

[45] T. Kanungo, D. M. Mount, N. S. Netanyahu, C. D. Piatko, R. Silverman, and A. Y. Wu, "An efficient k-means clustering algorithm: Analysis and implementation," *IEEE Transactions on Pattern Analysis and Machine Intelligence*, vol. 24, no. 7, pp. 881–892, 2002.

[46] J. C. Dunn, "A fuzzy relative of the ISODATA process and its use in detecting compact well-separated clusters," *Journal of Cybernetics*, vol. 3, no. 3, pp. 32–57, 1973.

[47] N. Otsu, "A threshold selection method from gray-level histograms," *IEEE Transactions on Systems, Man and Cybernetics*, vol. 9, no. 1, pp. 62–66, 1979.

[48] Y. Ma, P. Hof, S. Grant, S. Blackband, R. Bennett, L. Slatest, M. McGuigan, and H. Benveniste, "A three-dimensional digital atlas database of the adult c57bl/6j mouse brain by magnetic resonance microscopy," *Neuroscience*, vol. 135, no. 4, pp. 1203–1215, 2005.

[49] Y. Ma, D. Smith, P. R. Hof, B. Foerster, S. Hamilton, S. J. Blackband, M. Yu, and H. Benveniste, "In vivo 3D digital atlas database of the adult

C57BL/6J mouse brain by magnetic resonance microscopy," *Frontiers in Neuroanatomy*, vol. 2, 2008.

[50] B. Likar, M. Viergever, and F. Pernus, "Retrospective correction of MR intensity inhomogeneity by information minimization," *IEEE Transactions on Medical Imaging*, vol. 20, no. 12, pp. 1398–1410, 2001.

[51] E. Geremia, O. Clatz, B. H. Menze, E. Konukoglu, A. Criminisi, and N. Ayache, "Spatial decision forests for MS lesion segmentation in multi-channel magnetic resonance images," *NeuroImage*, vol. 57, no. 2, pp. 378–390, 2011.

[52] S. Sandor and R. Leahy, "Surface-based labeling of cortical anatomy using a deformable atlas," *IEEE transactions on medical imaging*, vol. 16, no. 1, pp. 41–54, 1997.

[53] S. M. Smith, M. Jenkinson, M. W. Woolrich, C. F. Beckmann, T. E. Behrens, H. Johansen-Berg, P. R. Bannister, M. De Luca, I. Drobnjak, D. E. Flitney *et al.*, "Advances in functional and structural MR image analysis and implementation as FSL," *Neuroimage*, vol. 23, pp. S208–S219, 2004.

[54] M. W. Woolrich, S. Jbabdi, B. Patenaude, M. Chappell, S. Makni, T. Behrens, C. Beckmann, M. Jenkinson, and S. M. Smith, "Bayesian analysis of neuroimaging data in FSL," *Neuroimage*, vol. 45, no. 1, pp. S173–S186, 2009.

[55] A. J. Schwarz, A. Gozzi, T. Reese, and A. Bifone, "In vivo mapping of functional connectivity in neurotransmitter systems using pharmacological MRI," *Neuroimage*, vol. 34, no. 4, pp. 1627–1636, 2007.